Measurement 247 (2025) 116805

Contents lists available at ScienceDirect

Measurement

journal homepage: www.elsevier.com/locate/measurement

Machine learning-empowered automatic analysis of distributed fiber optic sensor data for monitoring coincident corrosion and cracks in pipelines

Yiming Liu [a], Ying Huang [b], Yi Bao [a,*]

[a] Department of Civil, Environmental and Ocean Engineering, Stevens Institute of Technology, Hoboken, NJ 07030, United States
[b] Department of Civil, Construction and Environmental Engineering, North Dakota State University, Fargo, ND 58105, United States

ARTICLE INFO

Keywords:
Distributed fiber optic sensors (DFOS)
Corrosion
Crack
Machine learning
Interacting anomalies
Structural health monitoring

ABSTRACT

Coincident crack and corrosion pose risks to pipelines and challenges for condition monitoring. This paper presents a machine learning-empowered approach for automatically analyzing strain data measured from distributed fiber optic sensors for monitoring coincident cracks and corrosion, which simultaneously influence distributed sensor data. This approach has been implemented to detect, locate, and discriminate coincident cracks and corrosion. The performance of the approach has been evaluated through laboratory experiments using steel pipelines equipped with distributed fiber optic sensors, considering factors such as spatial resolution and sensor deployment methods. The experimental results showed that the proposed approach achieved high mAP@0.5 (0.935) and F1 score (0.920) in detecting and locating coincident cracks and corrosion, and less than 0.009 s in analyzing a strain profile with more than 500 data. This research provides valuable insights into real-time monitoring of interacting anomalies and addresses the practical data analysis challenges associated with massive sensor data analysis.

1. Introduction

Pipelines form the backbone of critical infrastructure networks, transporting vital resources like oil and gas across vast distances [1]. In the United States, over a million miles of natural gas pipelines connect production areas to distribution networks, ensuring a steady flow of energy [2]. Maintaining pipeline integrity is paramount for public safety, environmental protection, and uninterrupted delivery of essential services. Pipelines are susceptible to various anomalies such as corrosion, cracks, and dents [3]. Anomalies that occur at the same location in a pipeline are called interacting anomalies, which have a higher likelihood of causing a failure than a single anomaly. The United States Pipeline and Hazardous Materials Safety Administration (PHMSA) highlighted the heightened risk posed by combined threats compared to individual ones, as different anomalies can accelerate anomaly development [3]. Notably, coincident corrosion and cracks can lead to catastrophic pipeline failures [4]. Therefore, the ability to proactively detect and analyze anomalies, particularly interacting anomalies, plays a pivotal role in risk assessment, maintenance planning, and optimizing pipeline service life.

Pipeline inspection and monitoring tasks have been conducted based on ground penetrating radars [5], magnetic flux leakage [6–8], eddy current [9], acoustic emission [10], and ultrasonic testing [11,12]. Ground penetrating radars have been used to detect underground pipelines [13], exhibiting a tradeoff between spatial resolution and inspection depth [14]. Magnetic flux leakage has been applied to detect cracks and debonding of coatings [6]; eddy current methods have been applied to identify and locate cracks in pipelines [9]; and acoustic and ultrasonic techniques have been applied to detect cracks [11,12]. These traditional techniques are effective for specific cases.

Meanwhile, distributed fiber optic sensors (DFOS) have shown unique advantages in pipeline monitoring [15,16], such as the immunity to electromagnetic interference, high sensitivity, high accuracy, small size, light weight, distributed sensing ability, and long operating distance. Due to these advantages, DFOS have been used to monitor pipeline conditions based on the measurement of strain and temperature distributions. For example, DFOS were deployed on the external surface of pipelines to measure strain distributions [16–20], and the strain distributions were utilized to analyze deformations [15], cracks [17], buckling [18], and corrosion [19,20], showing high spatial resolution and high sensitivity simultaneously. Recently, DFOS have been utilized to monitor interacting bending and corrosion in pipelines [21]. In

* Corresponding author.
E-mail address: yi.bao@stevens.edu (Y. Bao).

https://doi.org/10.1016/j.measurement.2025.116805
Received 1 May 2024; Received in revised form 8 January 2025; Accepted 18 January 2025
Available online 20 January 2025

addition, DFOS have been applied to monitor steel-concrete composite cracks [22], and steel corrosion [23,24], and coincident crack and corrosion [25] in a broader spectrum of civil structures and materials [26,27], showing important advantages.

However, analyzing DFOS data is challenging because DFOS usually provides a large volume of data given the long sensor length. In an DFOS, measurements are continuously made along the length of the DFOS, different from discrete sensors that only provide measurements at individual spots where sensor nodes are deployed. When the sampling resolution is set to 0.65 mm [28], a meter-long sensor will produce more than 1500 data points per measurement. If the sampling frequency is set at 1 Hz, the meter-long sensor will produce more than 5.5 million data points per hour. In civil infrastructure applications, the length of DFOS can be 100 km or longer. Although the spatial resolution can be reduced in some applications, the data volume is still large, posing challenges to data analysis. Recent research has shown that the reduction in spatial resolution may result in missing information about anomalies, such as cracks [29].

A practical approach to reduce data volume is to use decimation techniques like data down-sampling when high-frequency data are unnecessary. However, those techniques do not overcome the challenges related to data analysis and interpretation. Identifying anomalies such as cracks and corrosion from DFOS data is still challenging, and manual analysis of data does not support real-time monitoring because manual data analysis is time-consuming. To overcome this challenge, machine learning techniques have been utilized to enable automatic analysis of DFOS data in monitoring cracks [17,30–32] and corrosion [20].

Motivated by the recent advances in machine learning approaches for automatic analysis of DFOS data, this research was conducted to achieve the ability to automate the analysis of DFOS data for monitoring interacting cracks and corrosion for pipelines, aiming at overcoming the challenge of analyzing massive DFOS data for real-time monitoring and management of pipelines. To this end, this research aims at: (1) developing a machine learning-based approach for analyzing DFOS data to determine crack and corrosion conditions in pipelines with coincident anomalies; and (2) discriminating strain changes caused by coincident cracks and corrosion for quantitative evaluation of pipeline conditions.

This research has three primary objectives: (1) enabling automatic analysis of DFOS data for monitoring coincident cracks and corrosion in pipelines through the development of a machine learning-based approach that considers the different spatial and temporal features of strain distributions related to cracks and corrosion; (2) understanding the effect of key variables of DFOS measurement and deployment pattern on the performance of the machine learning approach through a parametric study on the variables; and (3) understanding the performance of different versions of YOLO models via comparing a modified YOLOv8 model with other widely used machine learning models, including YOLOv3, YOLOv4, YOLOv5, and regular YOLOv8 models.

The remainder of the paper is organized as follows: Section 2 presents the machine learning approach developed in this research. Section 3 introduces the laboratory experiments designed to implement the approach and evaluate the performance of the approach. Section 4 presents and discusses the experimental results. Section 5 summarizes the new findings of this research.

2. Methodology

2.1. Framework

The framework of the machine learning approach is shown in Fig. 1, consisting of four main steps: (1) Strain distributions are measured using DFOS (Section 2.2). (2) Strain distributions are converted into graphs (Section 2.3). (3) Graphs are analyzed using a machine learning model to determine cracks and corrosion (Section 2.4). (4) Strain signatures of corrosion and cracks are decoupled (Section 4.5).

2.2. Data acquisition

A single-mode fiber optic cable, such as Corning® SMF-28e+® [33], can be utilized as both a distributed sensor and transmission line. The

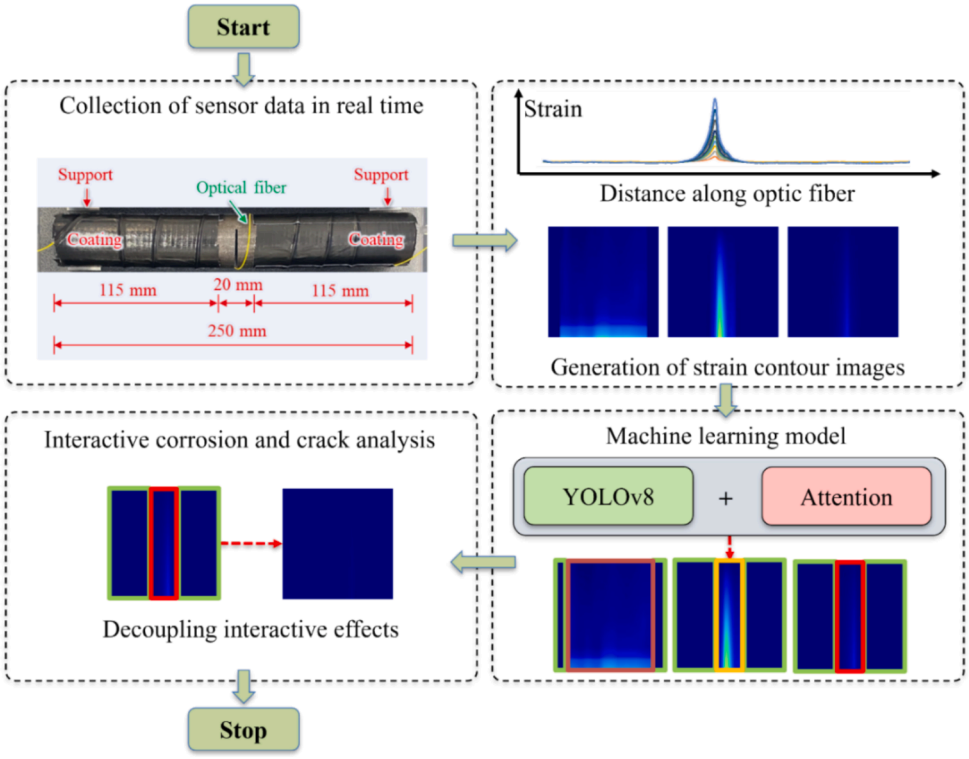

Fig. 1. Framework of the proposed machine learning-based approach for sensor data analysis.

fiber optic cable was composed of a glass core (diameter: 8.2 μm), a glass cladding (outer diameter: 125 μm), a dual-layer coating (outer diameter: 245 μm), and a tight buffer (outer diameter: 900 μm) for mechanical protection. The selection of this type of fiber optic cable was primarily based on its wide availability, high cost-effectiveness, and high performance in structural health monitoring (SHM) applications [20]. Light waves propagate along the fiber optic cable through total internal reflection at the core-cladding interface. Various distributed sensing technologies have been developed based on light scatterings in fiber optic cables. For example, optical frequency domain reflectometry (OFDR) has been developed to measure strain and temperature distributions with high spatial resolution and sampling frequency. Strain and temperature changes can be determined according to the following equation [17]:

$$\Delta\varepsilon_{OFDR} = \frac{\frac{\Delta f}{f} - k_T \Delta T_{OFDR}}{k_\varepsilon} \tag{1}$$

where $\Delta\varepsilon_{OFDR}$ and ΔT_{OFDR} are the strain and temperature changes, respectively; Δf and f are the frequency shift and average optical frequency, respectively; k_T and k_ε are the temperature and strain sensitivity coefficients, respectively, which are calibrated prior to applications.

In this study, a Luna ODiSI 6120 instrument was used to measure strains based on OFDR [34]. The measurement accuracy specified by the manufacturer is ± 5 με for strain [34]. The range of spatial resolution was 0.65 mm to 10.4 mm. The maximum length of fiber optic cable used as a sensor to obtain the strain profiles was 100 m [38], and the length of the stand-off cable was 200 m. This sensor length is sufficient for laboratory experiments and field testing of critical parts such as the connections of pipelines. When a longer sensor length is needed, alternative distributed sensing technologies like Brillouin scattering-based technologies can be considered [35]. Brillouin scattering-based technologies like Brillouin Optical Time Domain Analysis (BOTDA) can achieve a sensing distance longer than 100 km, but the spatial resolution is usually limited to a meter scale. High-resolution BOTDA technologies like Pulse-Pre-Pump BOTDA (PPP-BOTDA) have been developed, but the spatial resolution is still limited to 20 mm [35]. A high spatial resolution is necessary for accurate measurement of cracks [29]. The frequency of data acquisition was set to 2 Hz in this research. This high frequency was unnecessary for this research, but the data were also used in another research which required high frequency. More details about OFDR are available in the reference [36].

2.3. Graphic representation

The strain distributions measured from DFOS are presented as strains versus the distance along DFOS in a scattered plot with lines. The scattered plot is converted into graphs to facilitate sensor data interpretation using machine learning models. The primary procedure of generating a graph for representing DFOS data is illustrated in Fig. 2. First, an arbitrary strain distribution in time-domain and spatial-domain can be expressed using a two-dimensional matrix:

$$\boldsymbol{\varepsilon_a} = \begin{bmatrix} \varepsilon_{1,1} & \varepsilon_{1,2} & \cdots & \varepsilon_{1,N} \\ \cdots & \cdots & \cdots & \cdots \\ \varepsilon_{M,1} & \varepsilon_{M,2} & \cdots & \varepsilon_{M,N} \end{bmatrix} \tag{2}$$

where M is the sampling number of a specific time period (i.e., time-domain), and N is the number of data points of the strain distribution (i.e., spatial domain). Second, in each row of the matrix, a total of Q strain values are inserted between each pair of adjacent data points through linear interpolation [37], as shown in Eq. (3). This interpolation step enhances the resolution of strain distribution, ensuring a smooth and detailed representation within the generated graph.

$$\boldsymbol{\varepsilon_b} = \begin{bmatrix} \varepsilon_{1,1} & \varepsilon^1_{1,1} & \cdots & \varepsilon^Q_{1,1} & \varepsilon_{1,2} & \cdots & \varepsilon_{1,N} \\ \cdots & \cdots & \cdots & \cdots & \cdots & \cdots & \cdots \\ \varepsilon_{M,1} & \varepsilon^1_{M,1} & \cdots & \varepsilon^Q_{M,1} & \varepsilon_{M,2} & \cdots & \varepsilon_{M,N} \end{bmatrix} \tag{3}$$

Third, the elements in matrix $\boldsymbol{\varepsilon_b}$ are mapped to red (R), green (G), and blue (B) components for each pixel in the graph, following the relationship defined in Eq. (4) to Eq. (6). The most used color gradient is usually shown in Fig. 3**(a)**. Blue represents low values, green represents medium values, and red represents high values. The exact mapping process is shown in the cube of Fig. 3**(b)**. Simply calculate where the

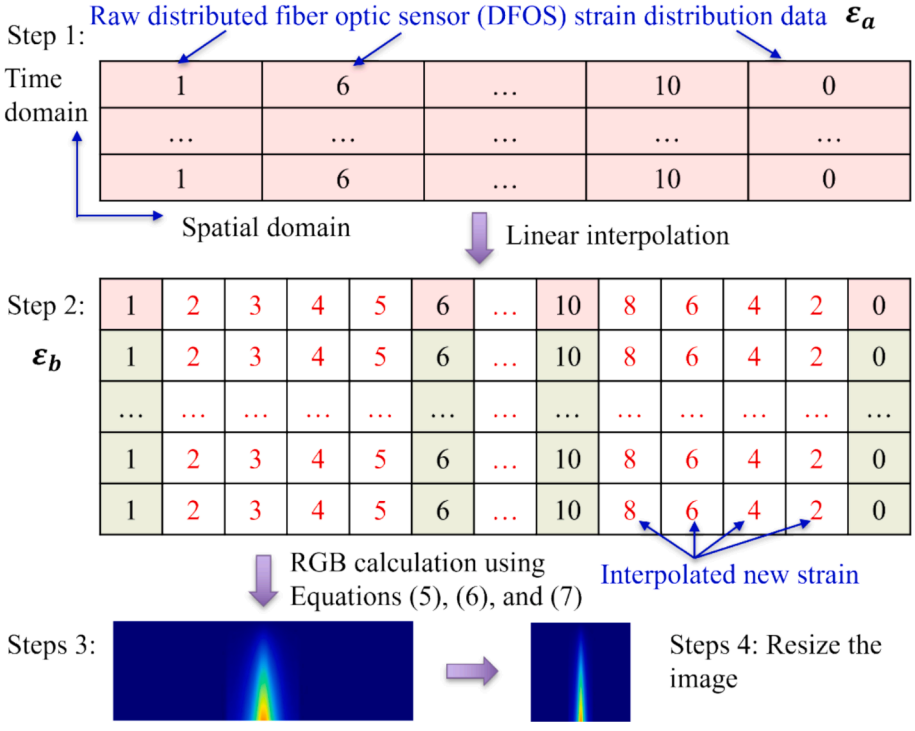

Fig. 2. Flowchart of generating intuitive contour images using distributed fiber optic sensor data.

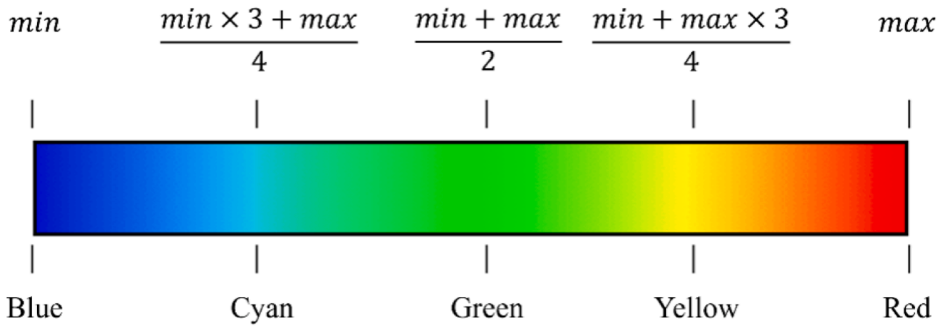

(a)

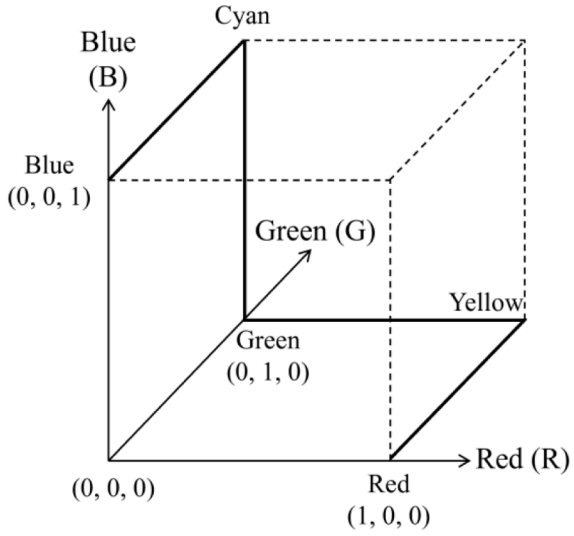

(b)

Fig. 3. Converting a number into a color gradient: (a) a common color gradient; and (b) RGB value mapping relationship cube.

RGB values appear on the folded lines in Fig. 3**(b)** to get the corresponding color values. More details about the equations for generating RGB graphs using numeric data are elaborated in reference [38].

$$R(\varepsilon)=255\begin{cases}0, \varepsilon<\varepsilon_{min}+0.5\Delta\varepsilon\\ \dfrac{4(\varepsilon-\varepsilon_{min}-0.5\Delta\varepsilon)}{\Delta\varepsilon}, \varepsilon_{min}+0.5\Delta\varepsilon\le\varepsilon<\varepsilon_{min}+0.75\Delta\varepsilon\\ 1, \varepsilon\ge\varepsilon_{min}+0.75\Delta\varepsilon\end{cases} \tag{4}$$

$$G(\varepsilon)=255\begin{cases}\dfrac{4(\varepsilon-\varepsilon_{min})}{\Delta\varepsilon}, \varepsilon<\varepsilon_{min}+0.25\Delta\varepsilon\\ 1, \varepsilon_{min}+0.25\Delta\varepsilon\le\varepsilon<\varepsilon_{min}+0.75\Delta\varepsilon\\ \dfrac{4(\varepsilon_{min}+\Delta\varepsilon-\varepsilon)}{\Delta\varepsilon}, \varepsilon\ge\varepsilon_{min}+0.75\Delta\varepsilon\end{cases} \tag{5}$$

$$B(\varepsilon)=255\begin{cases}1, \varepsilon<\varepsilon_{min}+0.25\Delta\varepsilon\\ \dfrac{4(\varepsilon_{min}+0.5\Delta\varepsilon-\varepsilon)}{\Delta\varepsilon}, \varepsilon_{min}+0.25\Delta\varepsilon\le\varepsilon<\varepsilon_{min}+0.5\Delta\varepsilon\\ 0, \varepsilon\ge\varepsilon_{min}+0.5\Delta\varepsilon\end{cases} \tag{6}$$

where ε is an arbitrary strain, and $\Delta\varepsilon=\varepsilon_{max}-\varepsilon_{min}$, where ε_{max} and ε_{min} are the maximum and minimum values, respectively. The RGB values are put into three matrices, respectively, which have the same dimensions as $\boldsymbol{\varepsilon_b}$.

Fourth, the RGB matrices are converted into a graph, which is a colored strain contour image (Fig. 2). Each contour image is sized into 640 × 640 pixels, which is the default resolution of input images for YOLOv8 [39]. The effect of image sizes was investigated in previous research [17].

2.4. Proposed machine learning model

The YOLOv8 algorithm was selected to develop the baseline model because of its exceptional performance in object detection tasks [40,41]. The architecture of YOLOv8 comprises three key components, which are an enhanced backbone network for feature extraction, a neck structure for efficient feature aggregation, and a detection head responsible for bounding box predictions and class probabilities [42]. The backbone component is based on the Cross Stage Partial (CSP) network [43], serving as the primary feature extractor to process the input strain contour image and generate a rich set of feature maps at various resolutions. The neck component collects feature maps from the backbone component [44]. The neck combines and refines these features across different scales, enhancing the ability to detect objects of varying sizes. The head in YOLOv8 takes the processed features from the neck and makes the final predictions [45]. The head is responsible for generating bounding boxes (locations and dimensions) and assigning different anomaly probabilities to each detected anomaly in the strain contour

images.

It is worth noting that an attention mechanism is added to the YOLOv8 model for improving object detection performance in this research. The original feature extraction network of YOLOv8 depends on the convolution layers, which extracts features from the input images but lacks the ability to handle massive measurements from DFOS used in large-scale structures such as pipelines [17]. In the proposed approach, a lightweight and efficient attention block, called convolutional block attention module (CBAM) [46], is added to the neck component to extract the features of strain contour images, as shown in Fig. 4.

This modification aims to guide the YOLOv8 model to focus on the most informative regions within feature maps, improving its ability to discriminate subtle details associated with corrosion, cracks, and coincident anomalies. The CBAM comprises both channel attention (C-Attention) and spatial attention (S-Attention). Given an intermediate feature map denoted as $\boldsymbol{F} \in \mathbb{R}^{C\times H\times W}$, CBAM sequentially infers a channel attention map $\boldsymbol{M_c} \in \mathbb{R}^{C\times 1\times 1}$ and a 2D spatial attention map $\boldsymbol{M_s} \in \mathbb{R}^{1\times H\times W}$ through the following equations:

$$\boldsymbol{F}' = \boldsymbol{M_c}(\boldsymbol{F}) \otimes \boldsymbol{F} \tag{7}$$

$$\boldsymbol{F}'' = \boldsymbol{M_s}(\boldsymbol{F}') \otimes \boldsymbol{F}' \tag{8}$$

where $\otimes$ is the element-wise multiplication, $\boldsymbol{F}'$ is the channel refined feature, and $\boldsymbol{F}''$ is the final refined feature. In multiplication, the attention values are broadcasted (copied) accordingly: channel attention values are broadcasted along the spatial dimension, and vice versa [46].

2.5. Evaluation metrics

The performance of the proposed machine learning approach has been evaluated using four popular metrics, which are precision [47], recall [47], F1 score [47], and mean average precision (mAP) [48]. The mathematical definitions of precision, recall, and F1 score are expressed using the following equations:

$$Precision = \frac{TP}{TP + FP} \tag{9}$$

$$Recall = \frac{TP}{TP + FN} \tag{10}$$

$$F1score = \frac{2 \times Precision \times Recall}{Precision + Recall} \tag{11}$$

where *TP* is the number of true positives (i.e., successful detection), *FP* is the number of false positives (i.e., false alarm), *FN* is the number of false negatives (i.e., miss), and *TN* is the number of true negatives (i.e., correct rejection). More details are elaborated in references [44,45].

Fig. 5 shows how the deep learning model detects anomalies and how accuracy is evaluated. When machine learning models are used to detect anomalies, anomalous areas are usually marked using anchor boxes, as shown in Fig. 5**(a)**, where the yellow boundaries represent anchor boxes serving as candidates for potential targets, and the red boundary represents the true anomaly area (ground truth box). The aim is to identify the yellow boundary that best represents the anomalous area. Intersection over union (IOU) is often used to evaluate the yellow candidate boxes [49]. IOU is the ratio of the overlap and union between the generated candidate bounding box and the ground truth bounding box, which measures the intersection of these two bounding boxes, as shown in Fig. 5**(b)**. The performance of the model improves as the IOU value increases, with higher IOU values indicating less difference between the generated candidate and ground truth bounding boxes.

The mAP is determined based on the IOU results, and both mAP@0.5 and mAP@0.5:0.95 have been considered: The mAP@0.5 is the mAP value when the IOU is higher than 0.5, and the mAP@0.5:0.95 is the average of mAP values when the IOU is from 0.5 to 0.95 with an interval of 0.05. IOU is a classical metric for evaluating the performance of the model for object detection.

3. Experimental program

3.1. Specimens

Experimental testing was conducted using steel pipe specimens subjected to coincident effects of corrosion and crack at the same positions. The specimens were made using carbon steel, which is commonly used for transmission pipelines transporting natural gas and hydraulic fluid according to ASTM 513 [50]. The length, diameter, and wall thickness of the pipe specimens were 250 mm, 38.1 mm, and 1.65 mm, respectively.

The pipe specimens were pre-processed using a saw to create notches in the middle section, as shown in Fig. 6. The notches were utilized to simulate the effect of cracks and control the positions of crack sections in the pipe specimens. The notch width was measured to be about 1.214 mm using a crack scope. The primary purpose of creating a notch is to enhance stress concentration in the pipe specimen and thus facilitate the initiation of a crack when the pipe specimen is loaded. Otherwise, without the notch, the pipe specimen would not crack and would fail with a dent at the loaded section [51].

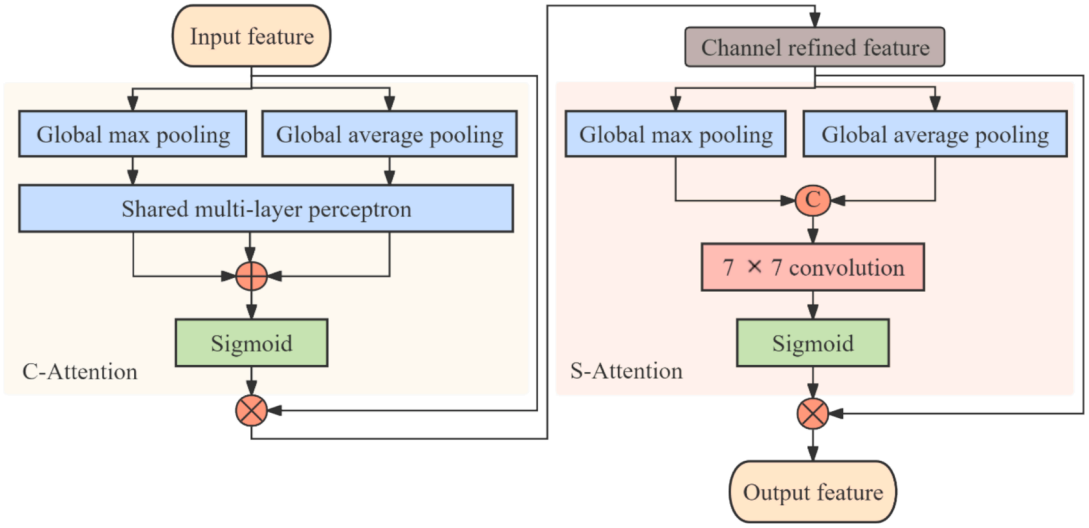

Fig. 4. Architecture of the convolutional block attention module integrating C- and S-Attention.

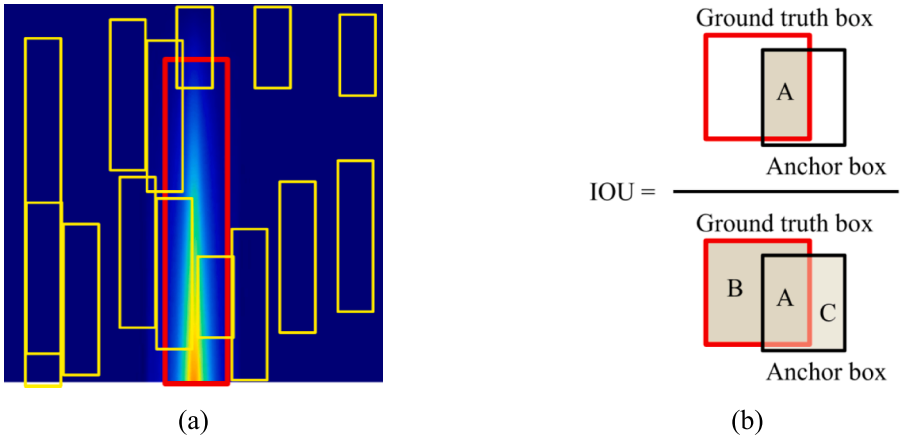

Fig. 5. Detection of anomaly areas using the deep learning method: (a) candidate boxes, and (b) the definition of IOU.

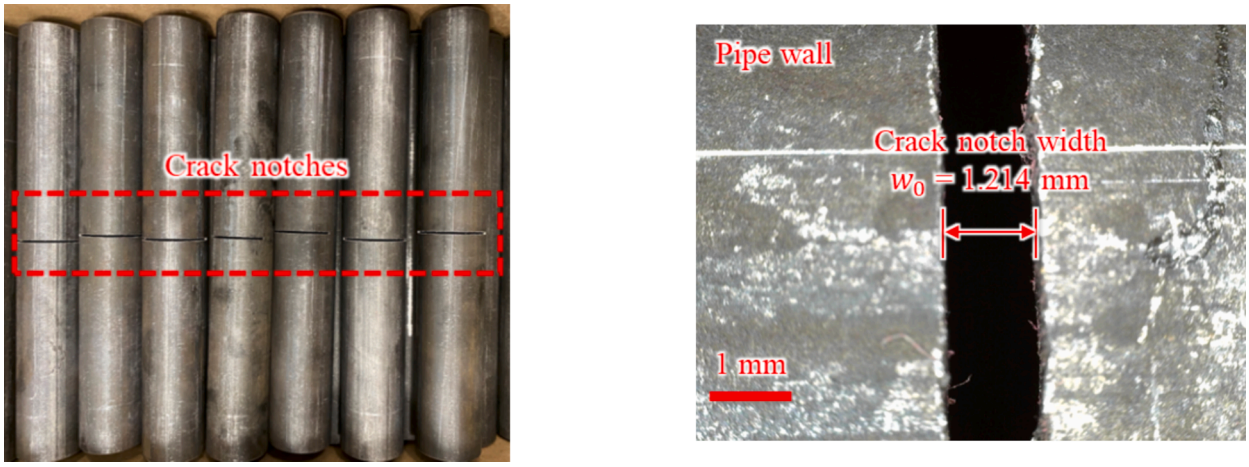

Fig. 6. Photos of pipeline specimens prepared through pre-crack tests for generating notches.

After the pipe specimens were notched, DFOS were attached to the surface of pipe specimens, passing over the notch, following the designed layout. Specifically, DFOSs were attached to the specimens following three steps. First, the fiber was held in place using paint tape at discrete spots along the length. Second, a fast-setting glue was applied at discrete points between the taped sections. After the glue set, the tape was carefully removed to avoid damaging the optical fibers or the newly applied adhesive. Before immersing the specimens, a low-viscosity two-part epoxy was applied to cover the fiber, creating a strong bond between the specimen and the fiber. The details about the specimens and sensor deployment schemes are shown in Table 1.

A total of 14 different cases were investigated, as listed in Table 1. These investigated cases were categorized into four groups, designated as C0 to C3. Group C0 only has one case, which was used as the reference case, and the specimen did not have a notch. Group C1 includes one specimen which was designed to investigate the effect of five measurement spatial resolutions of DFOS, which are 0.65 mm, 1.30 mm, 2.60 mm, 10.40 mm, and 20.80 mm. Group C2 includes four specimens that were designed to investigate the effect of four crack widths, which are 0.369 mm, 0.480 mm, 0.608 mm, and 0.762 mm. Group C3 consists of five specimens designed to investigate four sensor deployment schemes, which include four helix patterns with different spacings (30 mm, 60 mm, 90 mm, and 120 mm) and a straight-line pattern. The "crack width increase" in Table 1 refers to the difference between the crack with after loading and the original width of crack notches. The loading process is described in detail in Section 3.2.

Table 1
Investigated cases for combination effect of crack and corrosion.

Group	Cases	Spatial resolution (mm)	Sensor deployment pattern	Adjacent helix spacing (mm)	Crack width increase (mm)
C0	1	0.65	Helix	30	0
C1	2	0.65	Helix	30	0.608
	3	1.3	Helix	30	0.608
	4	2.6	Helix	30	0.608
	5	5.2	Helix	30	0.608
	6	10.4	Helix	30	0.608
	7	20.8	Helix	30	0.608
C2	8	0.65	Helix	30	0.369
	9	0.65	Helix	30	0.480
	10	0.65	Helix	30	0.762
C3	11	0.65	Helix	60	0.608
	12	0.65	Helix	90	0.608
	13	0.65	Helix	120	0.608
	14	0.65	Straight line	–	0.608

3.2. Experiments

The experiments were conducted in three main steps. First, the steel pipe specimens were loaded under three-point bending to increase the crack width at the mid-span section using a universal load frame (brand: Instron), as shown in Fig. 7. The distance between the two supports was 210 mm. The bending experiment was conducted under the displacement control mode with a displacement rate of 1 mm/min. The applied load was recorded by the load cell of universal testing machine, and an extensometer was instrumented to record the mid-span deflection of pipe specimens. The specimens were loaded under three-point bending to different displacements for generating different crack widths, as shown in Fig. 7**(b)**. In Fig. 7**(b)**, all load–displacement curves consist of the loading part and the unloading part. All curves showed similar curves with three stages: (1) Stage 1: from "O" to "A", where the bending load approximately linearly increases with the displacement. (2) Stage 2: from "A" to "B", where the bending load increases with the displacement with a decreasing slope until reaching the peak load at point B. Both Stages 1 and 2 belong to the loading part. (3) Stage 3: from "B" to "C" belonging to the unloading part, where the unloading force decreases with the unloading displacement. Strain distributions were measured from the DFOS throughout the loading process. This step was to create realistic crack widths that could simulate field conditions, where pipelines often experience mechanical stress and cracks before being subjected to corrosion.

Second, a two-part epoxy was applied to the pipe specimens to simulate the effect of coatings of real pipelines on corrosion protection. The application of epoxy isolated the surface of the pipe specimens from the atmosphere at both ends within a length of 115 mm, aiming to concentrate steel corrosion in the segment near the mid-span section of the specimen. Then, waterproof duct tapes were applied to the surface of epoxy for further corrosion protection, as shown in Fig. 8**(a)**.

Finally, the pipe specimens were put in a plastic container filled with a sodium chloride (NaCl) solution (concentration: 3.5 % by mass) for corrosion tests at room temperature (25 ± 2 °C). The test setup is shown in Fig. 8**(b)** and Fig. 8**(c)**. Each pipe specimen was supported by two plastic blocks at the two ends to expose the bottom of the pipes to the sodium chloride solution. The fiber optic cable was connected to the ODISI instrument for data acquisition. Each measurement took about 20 s, and the measurement frequency was 2 Hz. The total immersion time was 290 h. No substantial impact of the sodium chloride solution on the material and functional integrity of the fiber was identified. The fiber's coating material and adhesive do not react with sodium chloride. Further research is needed to understand the long-term durability.

4. Results and discussion

4.1. Strain distributions

Representative visual inspection results for each group of specimens are shown in Fig. 9**(a)**. Rust was generated on the external surfaces of pipes in groups C0 to C3. As the immersion time increased, the thickness of rust increased. Most rust concentrated to the notches, and only a small volume of rust fell off the pipes. The strain distributions measured from

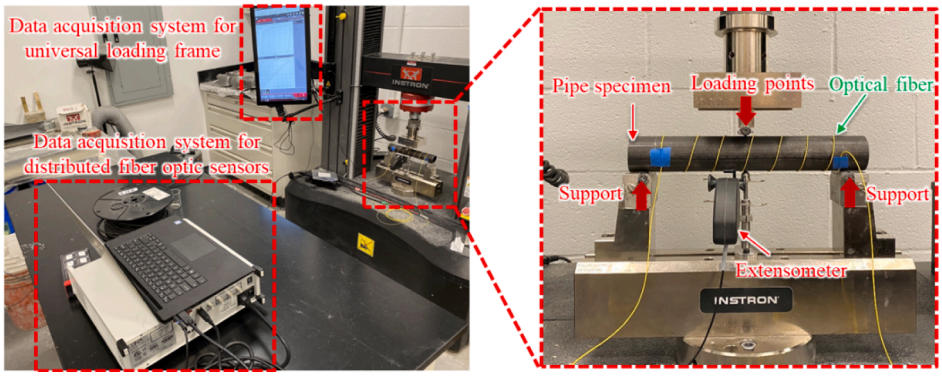

(a)

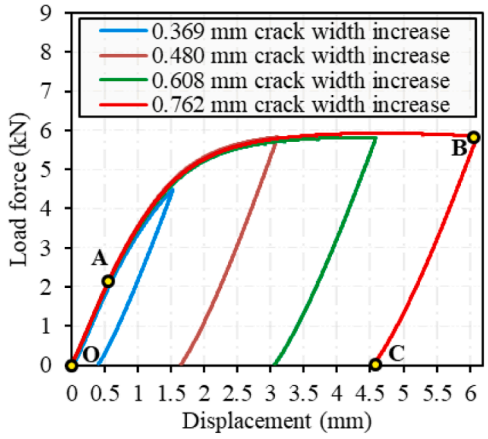

(b)

Fig. 7. Three-point bending test: (a) photograph for specimen preparation, instrumentation, and test set-up of the pre-dent test; and (b) load–displacement of the pipe specimens for generating different crack widths.

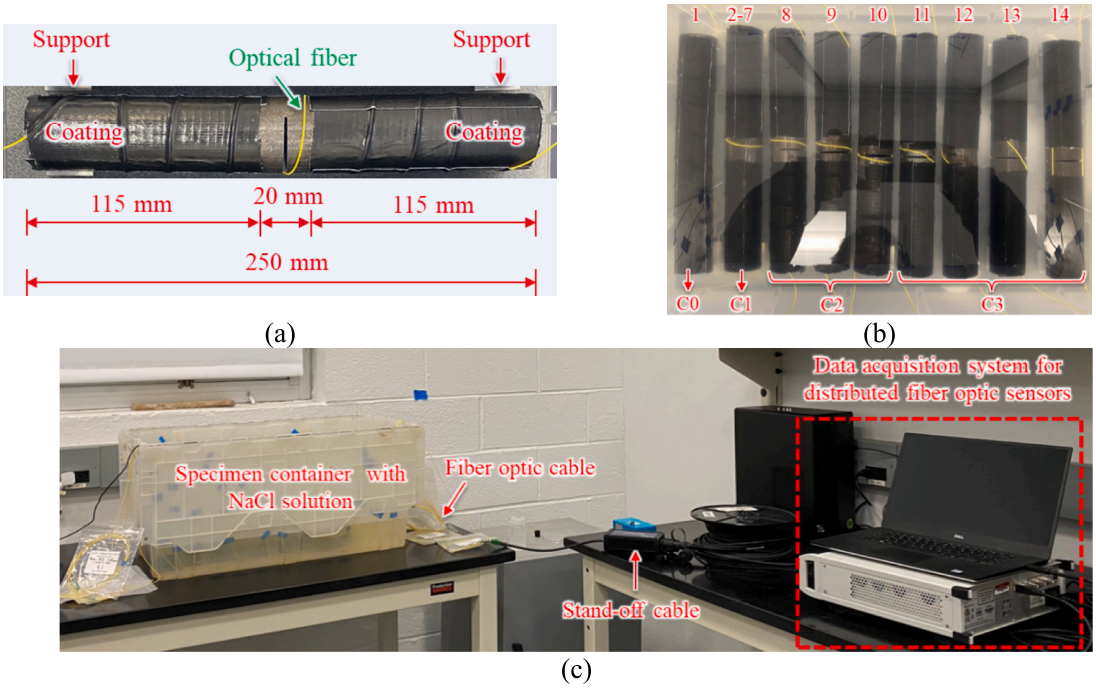

Fig. 8. Corrosion test of steel pipe specimens: (a) a notched pipe instrumented with distributed sensors; (b) the pipe specimens immersed in salt water; and (c) test set-up.

DFOS before the corrosion test were adopted as the reference for each specimen. According to previous research [36], when corrosion occurred, the pipe diameter increased due to the production of porous, expansive rust, thereby increasing tensile strains in the pipe.

Fig. 9 shows the strain distributions measured from DFOS at different time instants (24 h, 51 h, 94 h, 120 h, 144 h, 192 h, 240 h, and 290 h) in the corrosion test. The control specimen C0 exhibited minimal strains, as shown in Fig. 9**(b)**, which is consistent with visual inspection. The small strain changes are attributed to the combined effect of residual strain and corrosion of steel pipes, with safe corrosion levels evaluated in accordance with the ASME B31G [52]. High peaks are observed from the other strain distributions due to the notches, and the peak magnitude increases with time due to the growth of rust. In group C1, the strain peaks increased from 100 to 1,000 με over the entire immersion period, as shown in Fig. 9**(c)**. Similarly, in group C2, the magnitude of the strain peaks increased with crack width, as shown in Fig. 9**(d) to 9(f)**. Additionally, in group C3, the strain peaks decreased from 1,000 to 700 με as the adjacent helix spacing of the fiber optic cables increased, as shown in Fig. 9**(g) to 9(j)**. While the straight-line deployment achieved similar strain peaks, it requires prior knowledge of the crack location, as sensors that do not pass through cracks will fail to detect significant strain changes. This limitation makes helix deployment patterns more versatile and effective for identifying anomalies in the absence of pre-existing information about their locations. The results demonstrate the relationship between crack width and changes of strain peak magnitude, as well as the influence of fiber optic cable spacing.

4.2. Datasets

The experimental data in Fig. 9 and previous experimental data were utilized to generate a dataset for developing a machine learning model. The dataset has been derived from three sources: (1) A total of 1,000 contour images that represent cracks from previous research [30]. (2) A total of 1,000 contour images representing corrosion from previous research [20]. (3) A total of 1,000 contour images representing coincident corrosion and crack from the experiments in this research. Fig. 10 shows representative contour images. A total of 3,000 strain contour images were manually labelled using *labelme* [53]. As shown in Fig. 10 **(d)**, the labelled regions were used as the ground truth values to evaluate the performance of the machine learning model. The metrics in Section 2.5 were employed for performance evaluation. The dataset was randomly divided into training (80 %) and validation (20 %) sets.

4.3. Training process

The machine learning model was coded in Python 3.8 and trained on the Google Colaboratory platform with powerful computational resources, including a 2.30-GHz Intel Xeon (R) CPU, 13-GB RAM, and a 15-GB Tesla K80 GPU. In the training task, a pretrained model based on transfer learning was employed to accelerate the training process and potentially improve generalization. The training process included 100 epochs for iterative model refinement and a 640-pixel image size to balance detail and computational efficiency. The batch size was automatically determined to optimize the training process based on available memory and the characteristics of the dataset. The Adam optimizer with a learning rate of 0.00125 and a momentum of 0.937 was used, which is suitable for small customized datasets [44]. The training progress is shown in Fig. 11, with the x-axis representing the epoch number and the y-axis indicating the training loss, showing desired converging performance. The trained machine learning model was then used to detect corrosion, cracks, and coincident anomalies from strain contour images unseen in the training process.

4.4. Identification of cracks and corrosion

After 100 epochs, the precision, recall, F1 score, mAP@0.5 and mAP@0.5:0.95 reached 0.912, 0.929, 0.920, 0.935, and 0.872, respectively. The detailed results of the detection and localization accuracy for each condition (normal condition, corrosion, cracks, coincident corrosion and cracks) are shown in Table 2. Overall, the accuracy for coincident corrosion and cracks is lower than the accuracy for the other conditions due to the complexity of coincident corrosion and cracks.

Three representative examples of ground truth and detection results are shown in Fig. 12. The results demonstrate that the proposed method

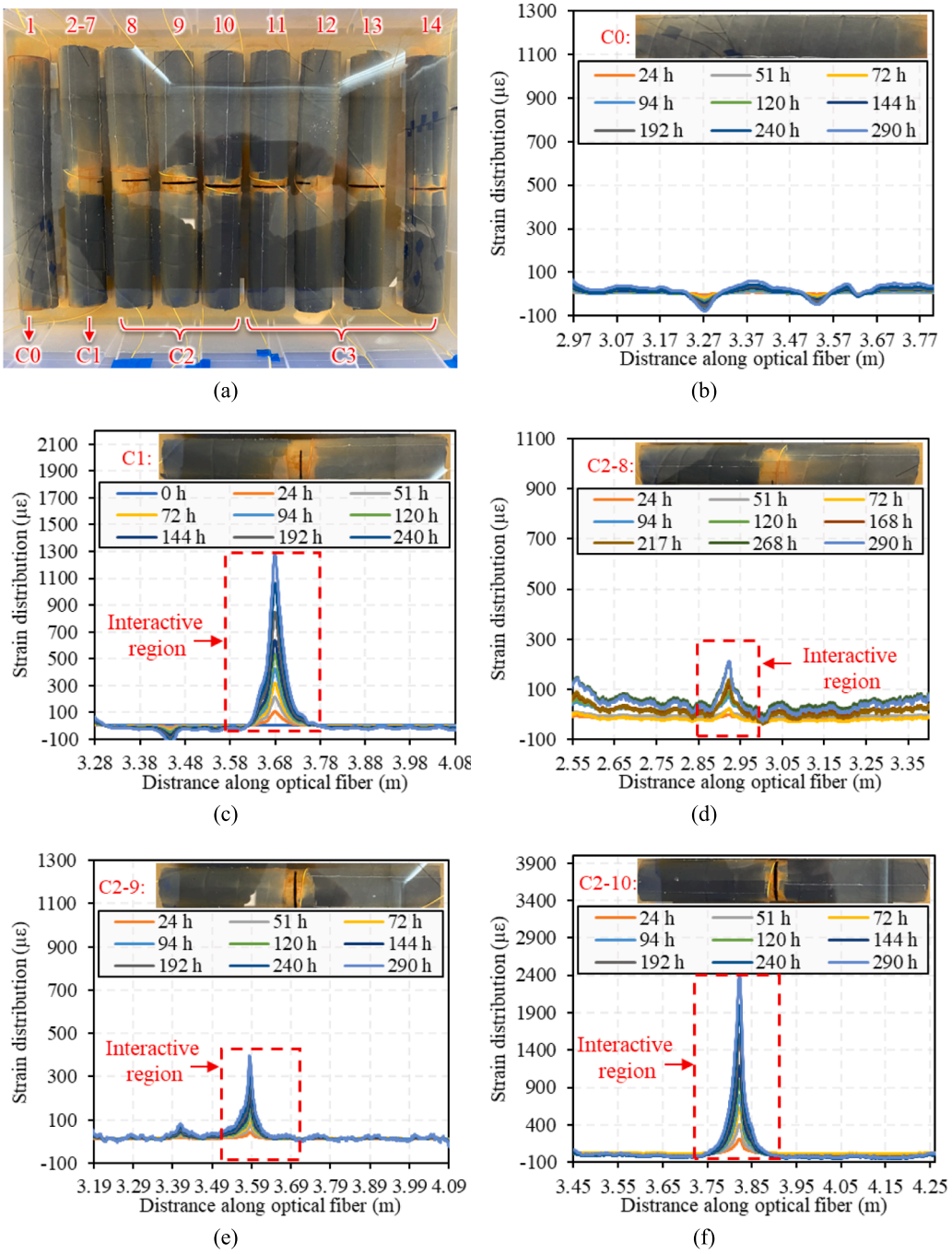

Fig. 9. Strain distributions measured from the distributed fiber optic strain sensors deployed along the pipe specimens: (a) visual inspection results; (b) Control case in group C0; (c) Cases 2–7 in group C1; (d) Case 8 in group C2; (e) Case 9 in group C2; (f) Case 10 in group C2; (g) Case 11 in group C3; (h) Case 12 in group C3; (i) Case 13 in group C3; and (j) Case 14 in group C3. The details of the cases can be found in Table 1.

has a good ability to detect and locate corrosion, cracks, and coincident corrosion and cracks.

The performance of the proposed machine learning method has been compared with other machine learning models, as listed in Table 3. These models were trained and evaluated using the same dataset. The modified YOLOv8 model achieved the highest accuracy. The comparison also reflects the benefits of the modifications of the YOLOv8 model. The YOLOv8 model achieved higher accuracy than the original YOLOv8 model. For example, the mAP@0.5:0.95 was increased from 0.837 to 0.872 (by 4.18 %). The computational efficiency of the different algorithms has been evaluated using the time required to analyze a contour image. The results show that YOLOv8-based models all run in less than 0.009 s per image, running faster than YOLOv3, YOLOv4 and YOLOv5 models, enabling real-time monitoring of pipeline conditions.

4.5. Discrimination of cracks and corrosion

The experimental data in Fig. 9**(c)** to Fig. 9**(j)** show pronounced interaction between cracks and corrosion. The presence of cracks accelerated the development of corrosion, and both cracks and corrosion affected the measured strained distributions. In this paper, an approach to decouple the contributions of crack and corrosion is presented. The

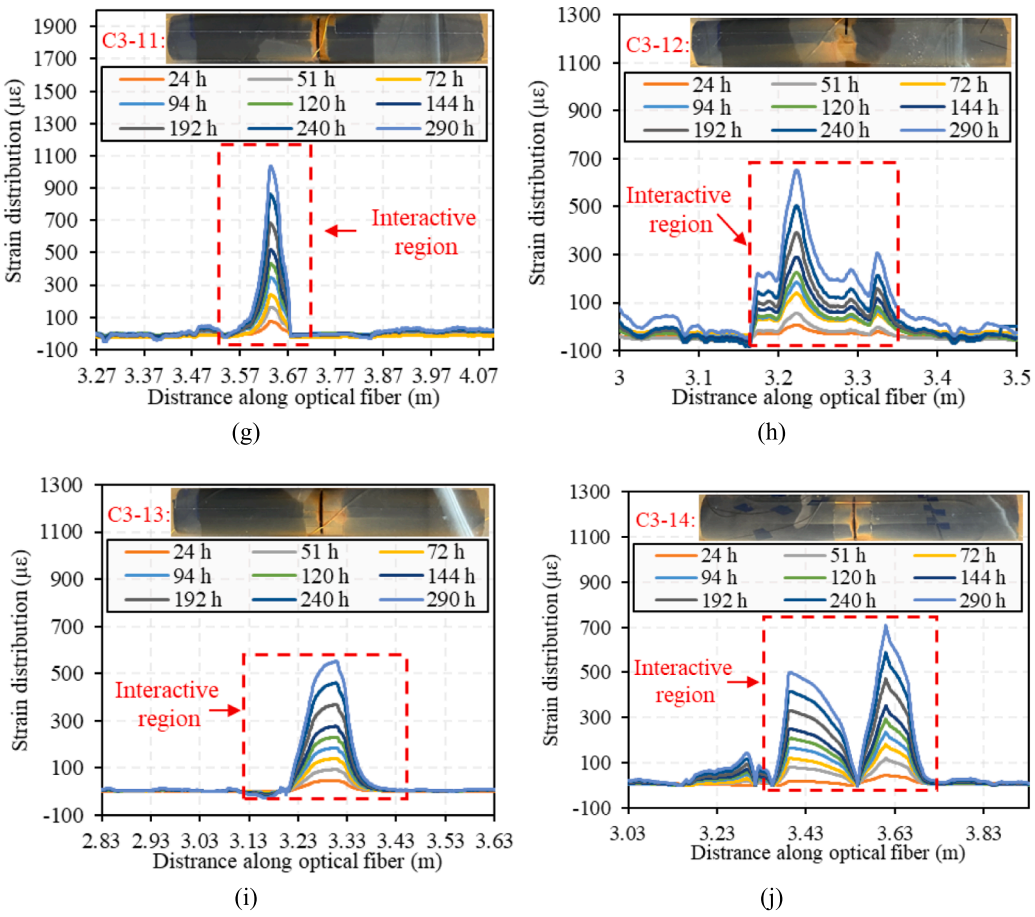

Fig. 9. (*continued*).

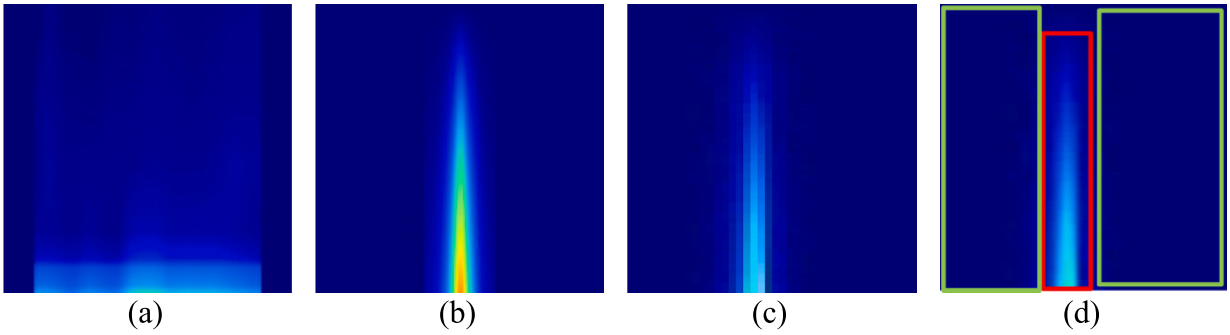

Fig. 10. Examples for the generated datasets: (a) corrosion image, (b) crack image, (c) image representing coincident corrosion and crack, and (d) labeled contour image.

development of this approach has been motivated by the distinct features of cracks and corrosion in strain distributions, as shown in Fig. 10. Cracks are abrupt localized events that cause sharp peaks in strain distributions measured from DFOS. More detailed information about the mechanical principles and the generation of sharp peaks caused by cracks are available in references [17,30,54].

Compared with cracks, corrosion is either a localized or a global event, and corrosion causes gradual strain changes often without sharp peaks. More detailed information about the mechanical principles and the development of strain changes caused by corrosion are available in references [36,55,56]. When cracks and corrosion coincide, the strain distribution measured from a distribution strain sensor is a combination of strains caused by cracks and corrosion, posing challenges in assessing pipeline conditions. The approach proposed to separate the contributions of cracks and corrosion has four primary steps:

1. The anomaly region representing coincident cracks and corrosion in a strain distribution is identified and located using the trained YOLOv8 model. A representative result of strain distribution is shown in Fig. 13**(a)**. The contour image of this strain distribution is shown in Fig. 13**(d)**. To highlight the coincident anomaly region, a contrast stretching algorithm [57] was applied to enhance the contrast of the intact region (Good) and anomaly region with both cracks and corrosion (Both), as shown in Fig. 13**(e)**.
2. In the anomaly region identified and located in step (1), the region is further divided into non-interactive and interactive regions, as shown in Fig. 13**(a)**. In a non-interactive region, either cracks or

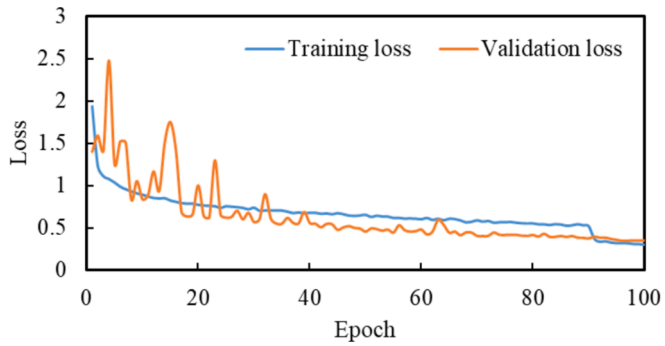

Fig. 11. Loss curves of the training and validation process of the proposed machine learning model.

Table 2
Performance of the proposed method for each type of anomaly.

Conditions	Precision	Recall	F1 score	mAP@0.5	mAP@0.5:0.95
Normal condition	0.895	0.939	0.916	0.979	0.863
Corrosion	0.931	0.938	0.934	0.931	0.931
Cracks	0.914	0.964	0.938	0.935	0.804
Coincident corrosion and cracks	0.910	0.876	0.893	0.892	0.888
All	0.912	0.929	0.920	0.935	0.872

corrosion exists; and in an interactive region, both of them exist and interact with each other.

3. The average strain value caused by corrosion in each non-interactive region is calculated to estimate the contribution of corrosion to strain changes, assuming that the strain change caused by corrosion is uniform, consistent with previous research [36]. The average strain is used to estimate the strain distribution within the adjacent interactive region, as shown in Fig. 13**(b)**. The red line indicates the average strain.
4. In the interactive region, the strain distribution is divided into the components standing for cracks and corrosion, separating the contributions of cracks and corrosion to the strain changes, as shown in Fig. 13**(c)**.

Following the above four steps, the strain distributions measured from DFOS can be analyzed to discriminate the contributions of cracks and corrosion for pipelines subjected to coincident anomalies. The cracks and corrosion conditions can then be utilized to guide the operation and maintenance efforts for pipelines.

4.6. *Limitations and future work*

Although this research proves the feasibility of using machine learning models for automatic analysis of DFOS data involving coincident cracks and corrosion, the proposed approach has not been validated using field tests. Additionally, more robust optical fiber sensors with reinforced or polyimide-coated fibers will be investigated, along with more complex mechanical states of pipelines to further evaluate the generalization performance of the proposed approach. Comprehensive field tests are necessary in future research. In field applications, pitting corrosion is common, and further research is necessary to distinguish between pitting corrosion and cracks. It should be noted that the strain distributions associated with pitting corrosion have slower growth rates compared with the strain distributions associated with cracks because corrosion is a slower process than cracking. The difference in time domain can be utilized to distinguish between cracks and pitting corrosion. Quantifying corrosion, such as through percent mass loss, will

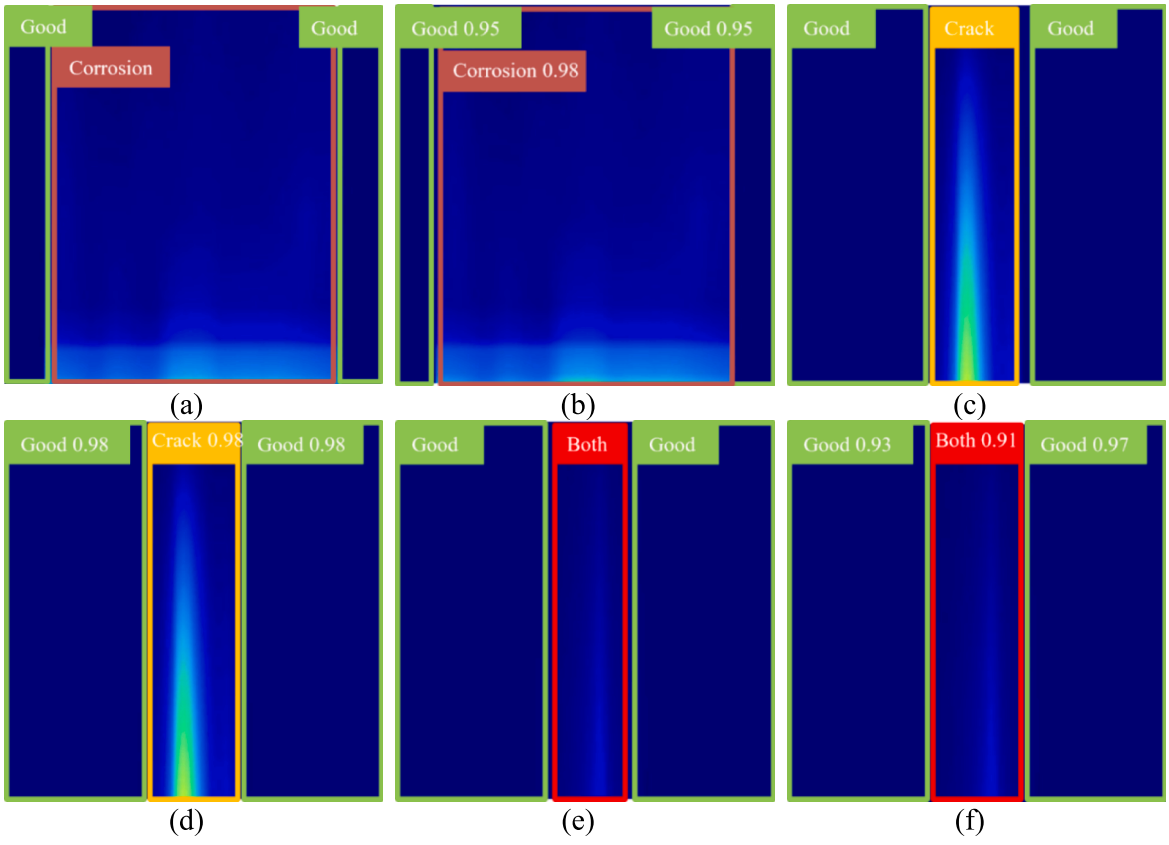

Fig. 12. Representative examples of the detection results for different anomalous conditions: (a) corrosion, (b) crack, and (c) coincident corrosion and crack.

Table 3
Performance comparison of different methods.

Algorithms	Precision	Recall	F1 score	mAP@0.5	mAP@0.5:0.95	Computation time (ms)
YOLOv3	0.857	0.868	0.862	0.856	0.649	28.2
YOLOv4	0.830	0.871	0.850	0.909	0.783	18.0
YOLOv5	0.868	0.873	0.870	0.875	0.811	9.1
YOLOv8s	0.883	0.878	0.880	0.920	0.837	8.6
YOLOv8s + SimAM	0.878	0.926	0.901	0.924	0.829	8.7
YOLOv8s + hyperparameter tunning	0.912	0.894	0.903	0.933	0.859	8.6
YOLOv8s + CBAM	0.897	0.937	0.917	0.929	0.865	8.7
YOLOv8s + CBAM + hyperparameter tunning	0.912	0.929	0.920	0.935	0.872	8.7

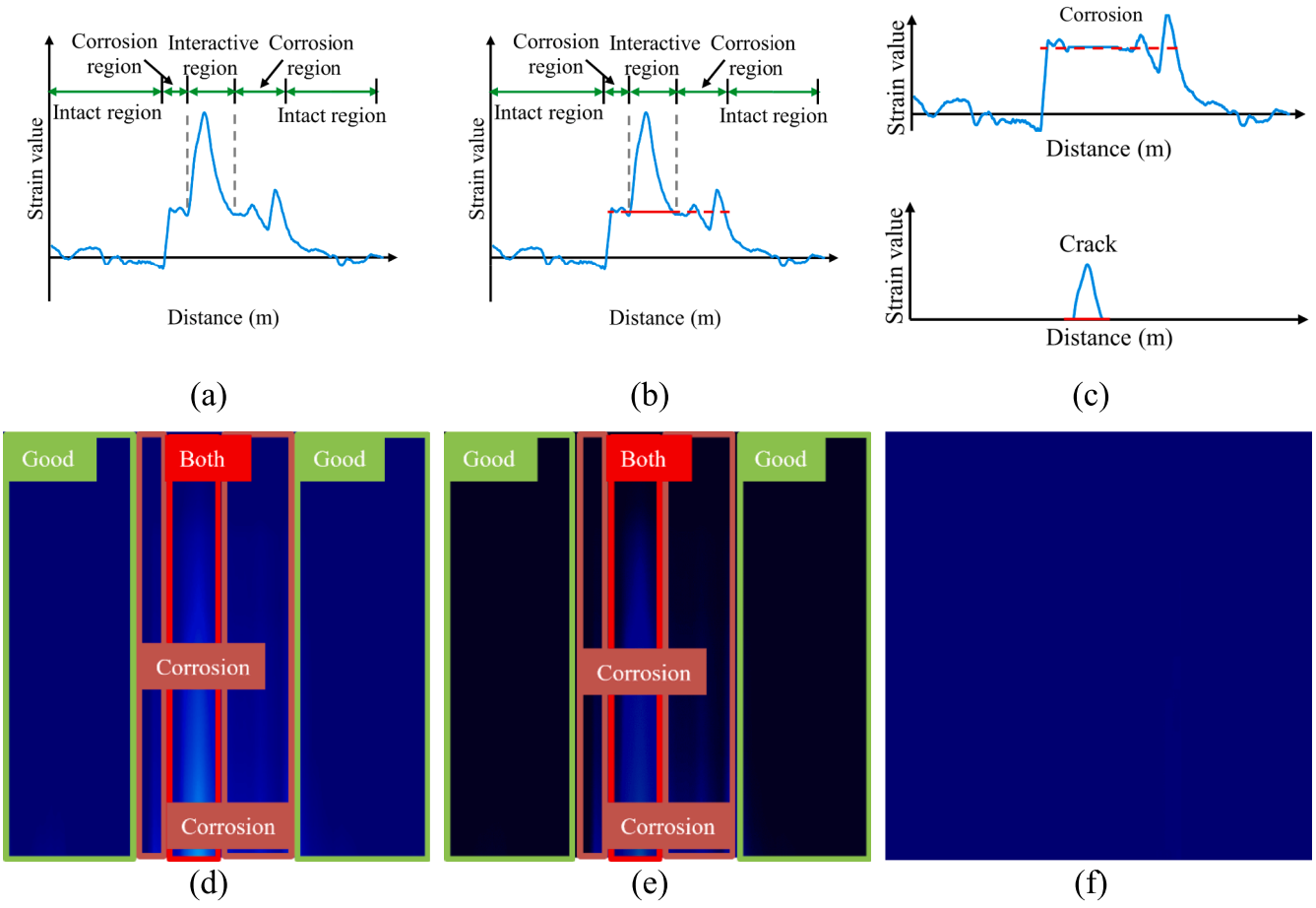

Fig. 13. Discrimination of strain changes caused by coincident cracks and corrosion: (a) a strain distribution involving coincident cracks and corrosion; (b) determination of the average strain; (c) discrimination of strains caused by cracks and corrosion; (d) a contour image; (e) an enhanced contour image after contrast stretching; and (f) a contour image after removal of the crack effect.

also be a priority in future studies to address the concern of varying corrosion levels.

The proposed method relies on the direct detection of strain changes by the DFOS. If the crack does not intersect with the sensor, the strain variations caused by the crack will not be captured, limiting the ability to detect the crack. Helix optimized deployment patterns can improve coverage to mitigate the limitation in crack detection. Another limitation is that the proposed method does not quantify cracks and corrosion. It will be useful to develop advanced methods for quantifying corrosion and cracks in future research.

In addition, in long-term monitoring of civil engineering structures, managing large volumes of DFOS data is a key challenge. A common approach is to use data decimation techniques, where the incoming data is down-sampled or selectively logged to reduce the data volume in applications where high-frequency sampling is not required, such as in static or slowly evolving conditions. However, in cases where real-time monitoring of dynamic events is critical such as sudden crack propagation or rapid corrosion onset, data decimation may risk missing key anomalies. In such scenarios, machine learning techniques offer a more robust and flexible solution. By analyzing the complete data set in real-time, machine learning algorithms can detect and differentiate between multiple types of anomalies, even in highly dynamic environments.

5. Conclusions

This paper presents a machine learning approach to automatically analyze strain distributions measured from DFOS used for monitoring pipelines subjected to coincident cracks and corrosion. The performance of the approach has been evaluated through laboratory experiments using pipeline specimens equipped with DFOS. The effects of spatial

resolution and sensor deployment schemes on the sensing performance have been evaluated. Based on the above investigations, the following conclusions are drawn:

- DFOS can be used to monitor coincident cracks and corrosion via measuring strain distributions of pipelines, because both cracks and corrosion can affect the strains in DFOS, enabling the detection and characterization of anomalies associated with the combined effects of cracks and corrosion.
- The proposed machine learning approach is effective in automatically analyzing the strain distributions measured from DFOS for detecting and locating coincident cracks and corrosion in pipelines. The experimental results showed that the proposed approach effectively detected and located cracks and corrosion, achieving the mAP@0.5 and F1 score of 0.935 and 0.920, respectively.
- The proposed approach for discriminating strain changes caused by coincident cracks and corrosion is useful for quantitative evaluation. With the discrimination approach, the strain distributions associated with cracks and corrosion can be determined and used for assessing pipeline conditions.

Further research is necessary to evaluate the generalization performance of the proposed approach. It is useful to re-train the machine learning model using field test data to improve the accuracy and generalizability of the model.

CRediT authorship contribution statement

Yiming Liu: Writing – review & editing, Writing – original draft, Visualization, Validation, Software, Resources, Methodology, Investigation, Formal analysis, Data curation. **Ying Huang:** Writing – review & editing, Validation, Funding acquisition, Conceptualization. **Yi Bao:** Writing – review & editing, Writing – original draft, Visualization, Validation, Supervision, Software, Resources, Project administration, Methodology, Investigation, Funding acquisition, Formal analysis, Data curation, Conceptualization.

Declaration of competing interest

The authors declare that they have no known competing financial interests or personal relationships that could have appeared to influence the work reported in this paper.

Acknowledgement

This research was funded by the United States Department of Transportation through PHMSA [grant numbers 693JK31950008CAAP, 693JK32310008POTA, and 693JK32450002CAAP] and United States National Science Foundation [grant number 2305882]. The contents of this paper do not reflect any opinion or endorsement of the sponsors. The authors thank Mr. Xiao Tan, a previous research assistant of the Smart Infrastructure Laboratory at Stevens Institute of Technology for his assistance with the laboratory experiments.

Data availability

Data will be made available on request.

References

[1] Y. Mahmood, J. Chen, N. Yodo, Y. Huang, Optimizing natural gas pipeline risk assessment using hybrid fuzzy bayesian networks and expert elicitation for effective decision-making strategies, Gas Sci. Eng. 125 (2024) 205283, https://doi.org/10.1016/j.jgsce.2024.205283.
[2] M.J. Gharabagh, H. Asilian, S.B. Mortasavi, A.Z. Mogaddam, E. Hajizadeh, A. Khavanin, Comprehensive risk assessment and management of petrochemical feed and product transportation pipelines, J. Loss Prev. Process Ind. 22 (2009) 533–539, https://doi.org/10.1016/j.jlp.2009.03.008.
[3] Y. Bao, Y. Huang, Distributed fiber optic sensor network for real-time monitoring of pipeline interactive anomalies. Report for the United States Department of Transportation Pipeline and Hazardous Materials Safety Administration, 2024.
[4] National Transportation Safety Board. Integrity management of gas transmission pipelines in high consequence areas. Ntsb/Ss-15/01 Pb2015-102735. 2015:253.
[5] A. Cataldo, E. De Benedetto, G. Cannazza, G. Leucci, L. De Giorgi, C. Demitri, Enhancement of leak detection in pipelines through time-domain reflectometry/ground penetrating radar measurements, IET Sci. Meas. Technol. 11 (2017) 696–702, https://doi.org/10.1049/iet-smt.2016.0310.
[6] Y. Shi, C. Zhang, R. Li, M. Cai, G. Jia, Theory and application of magnetic flux leakage pipeline detection, Sensors 15 (2015) 31036–31055, https://doi.org/10.3390/s151229845.
[7] B. Liu, Y. Cao, H. Zhang, Y.R. Lin, W.R. Sun, B. Xu, Weak Magnetic Flux Leakage: A Possible Method for Studying Pipeline Defects Located either inside or outside the Structures 74 (2015) 81–86, https://doi.org/10.1016/j.ndteint.2015.05.008.
[8] Y. Ege, M. Coramik, A new measurement system using magnetic flux leakage method in pipeline inspection, Measurement 123 (2018) 163–174, https://doi.org/10.1016/j.measurement.2018.03.064.
[9] Z. Chu, Z. Jiang, Z. Mao, Y. Shen, J. Gao, Low-power eddy current detection with 1-1 type magnetoelectric sensor for pipeline cracks monitoring, Sens. Actuators, A 318 (2021) 112496, https://doi.org/10.1016/j.sna.2020.112496.
[10] T.B. Quy, J.M. Kim, Crack detection and localization in a fluid pipeline based on acoustic emission signals, Mech. Syst. Sig. Process. 150 (2021) 107254, https://doi.org/10.1016/j.ymssp.2020.107254.
[11] G. Bernasconi, G. Giunta, Acoustic detection and tracking of a pipeline inspection gauge, J. Pet. Sci. Eng. 194 (2020) 107549, https://doi.org/10.1016/j.petrol.2020.107549.
[12] Y. Yu, A. Safari, X. Niu, B. Drinkwater, K.V. Horoshenkov, Acoustic and ultrasonic techniques for defect detection and condition monitoring in water and sewerage pipes: A review, Appl. Acoust. 183 (2021) 108282, https://doi.org/10.1016/j.apacoust.2021.108282.
[13] H. Bai, J.V. Sinfield, Improved background and clutter reduction for pipe detection under pavement using Ground Penetrating Radar (GPR), J. Appl. Geophys. 172 (2020), https://doi.org/10.1016/j.jappgeo.2019.103918.
[14] C. Yuan, H. Cai, Spatial reasoning mechanism to enable automated adaptive trajectory planning in ground penetrating radar survey, Autom. Constr. 114 (2020) 103157, https://doi.org/10.1016/j.autcon.2020.103157.
[15] B. Bednarz, P. Popielski, R. Sieńko, T. Howiacki, Ł. Bednarski, Distributed fibre optic sensing (DFOS) for deformation assessment of composite collectors and pipelines, Sensors 21 (2021) 5904, https://doi.org/10.3390/s21175904.
[16] M. Li, X. Feng, Y. Han, Brillouin fiber optic sensors and mobile augmented reality-based digital twins for quantitative safety assessment of underground pipelines, Autom. Constr. 144 (2022) 104617, https://doi.org/10.1016/j.autcon.2022.104617.
[17] Y. Liu, Y. Bao, Intelligent monitoring of spatially-distributed cracks using distributed fiber optic sensors assisted by deep learning, Measurement 220 (2023) 113418, https://doi.org/10.1016/j.measurement.2023.113418.
[18] X. Feng, W. Wu, X. Li, X. Zhang, J. Zhou, Experimental investigations on detecting lateral buckling for subsea pipelines with distributed fiber optic sensors, Smart Struct. Syst. 15 (2015) 245–258. https://doi.org/10.12989/sss.2015.15.2.245.
[19] L. Fan, Y. Bao, Review of fiber optic sensors for corrosion monitoring in reinforced concrete, Cement and Concrete Composites 120 (2021) 104029, https://doi.org/10.1016/j.cemconcomp.2021.104029.
[20] Y. Liu, X. Tan, Y. Bao, Machine learning-assisted intelligent interpretation of distributed fiber optic sensor data for automated monitoring of pipeline corrosion, Measurement 226 (2024) 114190, https://doi.org/10.1016/j.measurement.2024.114190.
[21] H. Lan, G. Ma, N.A. Hoult, I.D. Moore, Stress concentrations due to simulated corrosion pits in buried metal pipes under longitudinal bending, J. Civ. Struct. Heal. Monit. 12 (2022) 785–796, https://doi.org/10.1007/s13349-021-00522-8.
[22] H. Bai, D. Guo, W. Wang, X. Tan, M. Yan, G. Chen, Y. Bao, Experimental investigation on flexural behavior of steel-concrete composite floor slabs with distributed fiber optic sensors, J. Build. Eng. 54 (2022) 104668, https://doi.org/10.1016/j.jobe.2022.104668.
[23] L. Xu, S. Shi, Y. Huang, F. Yan, X. Yang, Y. Bao, Corrosion monitoring and assessment of steel under impact loads using discrete and distributed fiber optic sensors, Opt. Laser Technol. 174 (2024), https://doi.org/10.1016/j.optlastec.2024.110553.
[24] M. Davis, N.A. Hoult, A. Scott, Distributed strain sensing to determine the impact of corrosion on bond performance in reinforced concrete, Constr. Build. Mater. 114 (2016) 481–491, https://doi.org/10.1016/j.conbuildmat.2016.03.205.
[25] N.A. Hoult, O. Ekim, R. Regier, Damage/Deterioration Detection for Steel Structures Using Distributed Fiber Optic Strain Sensors, J. Eng. Mech. 140 (2014), https://doi.org/10.1061/(asce)em.1943-7889.0000812.
[26] M. Zeng, H. Chen, J. Ling, H. Zhao, D. Wu, Monitoring of prestressing forces in cross-tensioned concrete pavements during construction and maintenance based on distributed optical fiber sensing, Autom. Constr. 142 (2022) 104526, https://doi.org/10.1016/j.autcon.2022.104526.
[27] R. Ou, L. Luo, K. Soga, Brillouin scattering spectrum-based crack measurement using distributed fiber optic sensing, Struct. Health Monit. (2021) 1–22, https://doi.org/10.1177/14759217211030913.
[28] X. Tan, J. Du, Q. Zhang, W. Meng, Y. Bao, Monitoring restrained shrinkage and cracks of ultra-high-performance concrete (UHPC) using distributed fiber optic

sensors, Constr. Build. Mater. 422 (2024) 135789, https://doi.org/10.1016/j.conbuildmat.2024.135789.
[29] X. Tan, Y. Bao, Measuring crack width using a distributed fiber optic sensor based on optical frequency domain reflectometry, Measurement 172 (2021) 108945, https://doi.org/10.1016/j.measurement.2020.108945.
[30] Y. Liu, Y. Bao, Automatic interpretation of strain distributions measured from distributed fiber optic sensors for crack monitoring, Measurement 211 (2023) 112629, https://doi.org/10.1016/j.measurement.2023.112629.
[31] Q. Song, C. Zhang, G. Tang, F. Ansari, Deep learning method for detection of structural microcracks by brillouin scattering based distributed optical fiber sensors, Smart Mater. Struct. 29 (2020), https://doi.org/10.1088/1361-665x/ab874e.
[32] Q. Song, Y. Chen, E. Abdoli Oskoui, Z. Fang, T. Taylor, G. Tang, X. Zhao, F. Ansari, Micro-crack detection method of steel beam surface using stacked autoencoders on massive full-scale sensing strains, Struct. Health Monit. 19 (2020) 1175–1187, https://doi.org/10.1177/1475921719879965.
[33] The Corning I. Corning® SMF-28e+® optical fiber production information 2023. https://www.corning.com/media/worldwide/coc/documents/Fiber/PI-1463-AEN.pdf (accessed May 1, 2023).
[34] Luna. ODiSI 6000 series: Optical distributed sensor interrogators data sheet 2022: 1–6. https://lunainc.com/sites/default/files/assets/files/data-sheet/Luna ODiSI 6000 Data Sheet.pdf (accessed July 1, 2023).
[35] Y. Bao, F. Tang, Y. Chen, W. Meng, Y. Huang, G. Chen, Concrete pavement monitoring with PPP-BOTDA distributed strain and crack sensors, Smart Struct. Syst. 18 (2016) 405–423. https://doi.org/10.12989/sss.2016.18.3.405.
[36] X. Tan, L. Fan, Y. Huang, Y. Bao, Detection, visualization, quantification, and warning of pipe corrosion using distributed fiber optic sensors, Autom. Constr. 132 (2021) 103953, https://doi.org/10.1016/j.autcon.2021.103953.
[37] Y. Luo, K. Lu, An online state of health estimation technique for lithium-ion battery using artificial neural network and linear interpolation, J. Storage Mater. 52 (2022) 105062, https://doi.org/10.1016/j.est.2022.105062.
[38] P. Bourke. RGB colour space 1995. http://paulbourke.net/miscellaneous/colourspace/ (accessed May 1, 2023).
[39] R. Sapkota, D. Ahmed, M. Churuvija, M. Karkee, Immature green apple detection and sizing in commercial orchards using YOLOv8 and shape fitting techniques, IEEE Access 12 (2024) 1, https://doi.org/10.1109/access.2024.3378261.
[40] M. Zhang, Z. Wang, W. Song, D. Zhao, H. Zhao, Efficient small-object detection in underwater images using the enhanced YOLOv8 network, Appl. Sci. 14 (2024) 1095, https://doi.org/10.3390/app14031095.
[41] M. Hussain, YOLO-v1 to YOLO-v8, the rise of YOLO and its complementary nature toward digital manufacturing and industrial defect detection, Machines. 11 (2023), https://doi.org/10.3390/machines11070677.
[42] W. Li, M.I. Solihin, H.A. Nugroho, RCA: YOLOv8-based surface defects detection on the inner wall of cylindrical high-precision parts, Arab. J. Sci. Eng. (2024), https://doi.org/10.1007/s13369-023-08483-4.
[43] C.Y. Wang, H.Y. Mark Liao, Y.H. Wu, P.Y. Chen, J.W. Hsieh, I.H. Yeh, CSPNet: A New Backbone that can Enhance Learning Capability of CNN, IEEE Computer Society Conference on Computer Vision and Pattern Recognition Workshops (2020) 390–391.
[44] R.Y. Ju, W. Cai, Fracture detection in pediatric wrist trauma X-ray images using YOLOv8 algorithm, Sci. Rep. 13 (2023) 1–13, https://doi.org/10.1038/s41598-023-47460-7.
[45] X. Zhu, S. Lyu, X. Wang, Q. Zhao, TPH-YOLOv5: Improved YOLOv5 based on transformer prediction head for object detection on drone-captured scenarios, in: Proceedings of the IEEE International Conference on Computer Vision, 2021, https://doi.org/10.1109/iccvw54120.2021.00312.
[46] S. Woo, J. Park, J.Y. Lee, I.S. Kweon, Convolutional block attention module, Lect. Notes Comput. Sci 11211 LNCS:3–19 (2018), https://doi.org/10.1007/978-3-030-01234-2_1.
[47] W. Wang, W. Hu, W. Wang, X. Xu, M. Wang, Y. Shi, S. Qiu, E. Tutumluer, Automated crack severity level detection and classification for ballastless track slab using deep convolutional neural network, Autom. Constr. 124 (2021) 103484, https://doi.org/10.1016/j.autcon.2020.103484.
[48] X. Yin, Y. Chen, A. Bouferguene, H. Zaman, M. Al-Hussein, L. Kurach, A deep learning-based framework for an automated defect detection system for sewer pipes, Autom. Constr. 109 (2020) 102967, https://doi.org/10.1016/j.autcon.2019.102967.
[49] X. Tan, Y. Bao, Q. Zhang, H. Nassif, G. Chen, Strain transfer effect in distributed fiber optic sensors under an arbitrary field, Autom. Constr. 124 (2021) 103597, https://doi.org/10.1016/j.autcon.2021.103597.
[50] ASTM International, Standard Specification for Electric-Resistance-Welded Carbon and Alloy Steel Mechanical Tubing. (2020), https://doi.org/10.1520/a0513_a0513m-20a.
[51] X. Tan, S. Poorghasem, Y. Huang, X. Feng, Y. Bao, Monitoring of pipelines subjected to interactive bending and dent using distributed fiber optic sensors, Autom. Constr. 160 (2024) 105306, https://doi.org/10.1016/j.autcon.2024.105306.
[52] The American Society of Mechanical Engineers (ASME) (2023).
[53] A. Torralba, B.C. Russell, J. Yuen, LabelMe: Online image annotation and applications, Proc. IEEE 98 (2010) 1467–1484, https://doi.org/10.1109/jproc.2010.2050290.
[54] X. Tan, A. Abu-Obeidah, Y. Bao, H. Nassif, W. Nasreddine, Measurement and visualization of strains and cracks in CFRP post-tensioned fiber reinforced concrete beams using distributed fiber optic sensors, Autom. Constr. 124 (2021), https://doi.org/10.1016/j.autcon.2021.103604.
[55] L. Fan, Y. Bao, W. Meng, G. Chen, In-situ monitoring of corrosion-induced expansion and mass loss of steel bar in steel fiber reinforced concrete using a distributed fiber optic sensor, Compos. B Eng. 165 (2019) 679–689, https://doi.org/10.1016/j.compositesb.2019.02.051.
[56] L. Fan, X. Tan, Q. Zhang, W. Meng, G. Chen, Y. Bao, Monitoring corrosion of steel bars in reinforced concrete based on helix strains measured from a distributed fiber optic sensor, Eng. Struct. 204 (2020) 110039, https://doi.org/10.1016/j.engstruct.2019.110039.
[57] M. Yang, T. Su, N. Pan, Y. Yang, Systematic image quality assessment for sewer inspection, Expert Syst. Appl. 38 (2011) 1766–1776, https://doi.org/10.1016/j.eswa.2010.07.103.